

## Electrical-resistivity characterization of an industrial site using long electrodes

Dale F. Rucker<sup>1</sup>, Meng H. Loke<sup>2</sup>, Marc T. Levitt<sup>1</sup>, and Gillian E. Noonan<sup>1</sup>

### ABSTRACT

An electrical-resistivity survey was completed at the T tank farm at the Hanford nuclear site in Washington State, U.S.A. The purpose of the survey was to define the lateral extent of waste plumes in the vadose zone in and around the tank farm. The T tank farm consists of single-shell tanks that historically have leaked and many liquid-waste-disposal facilities that provide a good target for resistivity mapping. Given that the site is highly industrialized with near-surface metallic infrastructure that potentially could mask any interpretable waste plume, it was necessary to use the many wells around the site as long electrodes. To accommodate the long electrodes and to simulate the effects of a linear conductor, the resistivity inversion code was modified to assign low-resistivity values to the well's location. The forward model within the resistivity code was benchmarked for accuracy against an analytic solution, and the inverse model was tested for its ability to recreate images of a hypothetical target. The results of the tank-farm field survey showed large, low-resistivity targets beneath the disposal areas that coincided with the conceptual hydrogeologic models developed regarding the releases. Additionally, in areas of minimal infrastructure, the long-electrode method matched the lateral footprint of a 3D surface-resistivity survey with reasonable fidelity. Based on these results, the long-electrode resistivity method may provide a new strategy for environmental characterization at highly industrialized sites, provided a sufficient number and density of wells exist.

### INTRODUCTION

The DC electrical-resistivity-characterization (ERC) method is an excellent tool for spatially defining highly saline pore water (Bevc and Morrison, 1991; LaBrecque et al., 2004; Singha and

Gorelick, 2005, 2006; Cassiani et al., 2006) and brackish groundwater (Nowroozi et al., 1999; Choudhury et al., 2001; Bauer et al., 2006; Pidlisecky et al., 2006; Koukadaki et al., 2007; Swarzenski et al., 2007). ERC is applied by placing small metallic electrodes on the surface or within boreholes, passing current on one pair of electrodes, measuring the resulting voltage potential (usually as transfer resistance) in another pair of electrodes, and inverting the data to build an image of the subsurface based on contrasts in electrical properties. ERC has been used extensively to map the subsurface of the Hanford nuclear site in eastern Washington, U.S.A. (e.g., Rucker and Fink, 2007; Rucker et al., 2009), where more than 454 million liters (120 million gal) of liquid waste composed of a concentrated electrolytic solution were discharged directly into the ground beginning in the mid-1940s (Gephart, 2003; Gee et al., 2007). Some of this liquid waste exceeded 5 mol/liter nitrate and 19 mol/liter sodium (Zachara et al., 2007). Rucker et al. (2009) report porewater conductivities above 180 mS/cm as a result of direct disposal.

Because of the high cost of drilling boreholes for placing vertical electrode arrays and conducting borehole-to-borehole ERC, resistivity is primarily applied at Hanford on the surface along parallel and orthogonal 2D lines (e.g., Rucker et al., 2005). Although the raw resistivity data are acquired in two dimensions, a 3D electrical-resistivity model can be constructed by properly georeferencing the electrode coordinates. Several isolated liquid-waste discharge sites have been characterized with 3D ERC in this manner (e.g., Rucker et al., 2009). The discharge sites are often located adjacent to groupings of large underground, concrete-supported metal storage tanks, familiarly called tank farms (Zachara et al., 2007). The T tank farm is surrounded by several liquid-waste discharge sites, including unlined cribs (concrete vaults with open bottoms) and trenches (long ditches). The tank farm was constructed between 1943 and 1944, and the tanks were filled to capacity soon after completion. The limited tank storage capacity forced liquid waste from the tank farm to be discharged to the surrounding areas into the cribs and trenches. Most of the cribs and all of the trenches received waste directly from the tanks as overflow (Waite, 1991).

Although ERC of the waste sites on the periphery of the tank

Manuscript received by the Editor 4 September 2009; revised manuscript received 14 November 2009; published online 30 September 2010.

<sup>1</sup>hydroGEOPHYSICS, Inc., Tucson, Arizona, U.S.A. E-mail: druck8240@gmail.com; mlevitt@hgiworld.com; gnoonan@hgiworld.com.

<sup>2</sup>Geotomo Software, Penang, Malaysia. E-mail: drmhloke@yahoo.com.

© 2010 Society of Exploration Geophysicists. All rights reserved.

farms has been successful, imaging unplanned releases of tank waste inside the tank farm is a much more difficult problem (Rucker et al., 2006). The waste-transfer pipelines, tanks, fences, and other metallic objects buried just under the surface cause the electric current to converge toward these more electrically conductive features, potentially making any surface-resistivity measurements uninterpretable (Vickery and Hobbs, 2002; Rucker, 2010). The near-surface infrastructure limits the electric current from flowing deeply into regions of the vadose zone where a waste plume would reside. To overcome the electrical interference from the infrastructure, current sources and voltage measurements should be placed far from the metal — ideally, below the buried tanks. Unfortunately, drilling inside a tank farm to place vertical electrode arrays is risky. Dome-load restrictions on the aging tanks and the waste-transfer pipelines limit where boreholes can be placed.

A trade-off between access to the deep vadose zone and minimal risk and expense is to use existing steel-cased wells as linear current-source and voltage-receiver electrodes. The waste-management area around the T tank farm has more than 100 wells completed in the vadose zone or used for groundwater monitoring that could be utilized as a well-to-well (WTW) resistivity imaging method. The term *WTW imaging* is not to be confused with *crosswell imaging*, which implements a set of vertically nested point electrodes. Ramirez et al. (1996) and Daily et al. (2004a) discuss the potential of linear sources, which they call *long electrodes*, to image waste plumes beneath Hanford's tank farms. Their experiments focus on a simulated tank leak within a three-quarters scaled mock tank environment using borehole-to-borehole ERC. The individual electrodes within the boreholes are fused together (i.e., wires from electrodes are connected) to form a metal casing analog. Daily et al. (2004b) also demonstrate the use of long-electrode ERC for reservoir characterization; Ramirez et al. (2003) discuss its use for monitoring carbon sequestration.

Motivated by previous work, we applied the linear source-and-receiver long-electrode array at the T tank farm to characterize the plumes below waste sites on the periphery of the farm as well as unintentional leaks from tanks inside the site. The field experiment described herein used actual steel well casings placed around the waste

sources. The linear sources and receivers of the WTW resistivity experiment are accommodated in the numerical resistivity model by assigning very conductive cells to the well's location. An example is shown, comparing the analytic solution for a linear current source and point-receiver electrode on the surface (no known analytic solution exists for WTW geometry). Furthermore, hypothetical examples are presented to demonstrate the potential advantage of WTW geometry. Lastly, the inverse model results from WTW are compared to the results of traditional surface electrode arrays collected in parallel and orthogonal directions over waste sites where metallic infrastructure is minimal.

## RESEARCH SITE

The T tank farm is in the northern portion of the 200 West area of the Hanford site near the T plant (Figure 1). The tank farm consists of twelve 100-series tanks ( $\sim 2000 \text{ m}^3$ ), four 200-series tanks ( $\sim 200 \text{ m}^3$ ), waste-transfer lines, and tank ancillary equipment. Figure 2 shows the distribution of facilities at the tank farm. The 100-series tanks are 23 m across, 9 m tall, and approximately 2.2 m from the surface of the ground down to the top of the tank. They are encased in a 0.3-m-thick concrete shell that was coated with asphalt to reduce corrosion of the tanks and to seal them from the surrounding soil. The four 200-series tanks are 6.1 m across and approximately 8 m tall. As noted in Figure 2, seven of the 100-series single-shell tanks (SSTs) in the tank farm are designated as assumed or confirmed leakers (Hanlon, 2005), with the largest leak from tank T-106 on the west side of the farm. The 200-series tanks are thought to be of higher integrity.

The results of field investigation and historical characterization activities have been used to develop a conceptual model for the nature and extent of contamination in the vadose zone beneath the T tank farm. Myers (2005) identifies two major contamination zones in the tank farm. The first zone, near tanks T-106 and T-103, results from the combined effects of an estimated 435,000-liter leak from tank T-106 and an 11,400-liter transfer line leak from tank T-103. The contaminant plume from these sources is estimated to be approximately 76 m in diameter, centered near the southeast quadrant of tank T-106 and extending to approximately 27–30 m below ground surface.

Historical process records indicate that waste losses from tank T-101, the second contamination zone, were the result of overfilling the tank by as much as 38,000 liters in 1969. Based on historical data and spectral gamma-ray logging, the contaminant plume from the tank leak extends to approximately 36.6 m below ground surface and has migrated in a southerly direction. Groundwater-monitoring data collected around the tank farm indicate that some contamination has reached the unconfined aquifer at a depth of approximately 70 m.

Several recent drilling and sampling activities within the tank farm have further characterized inorganic contamination in the vadose zone. These include boreholes C4104 and C4105 near tank T-106 and well W11-39, outside the fence surrounding the farm (Figure 3). In general, sulfate and nitrate concentrations are highest close to the tanks and the liquid-waste disposal areas. For example, a spike of nitrate was measured 33–36 m below ground surface (20 m below the bottom of tank T-106).

To the west and northeast of the tank farm, several waste sites received large quantities of electrolytic liquid waste as direct disposal to the ground. Most of the liquid was received on the west side of the

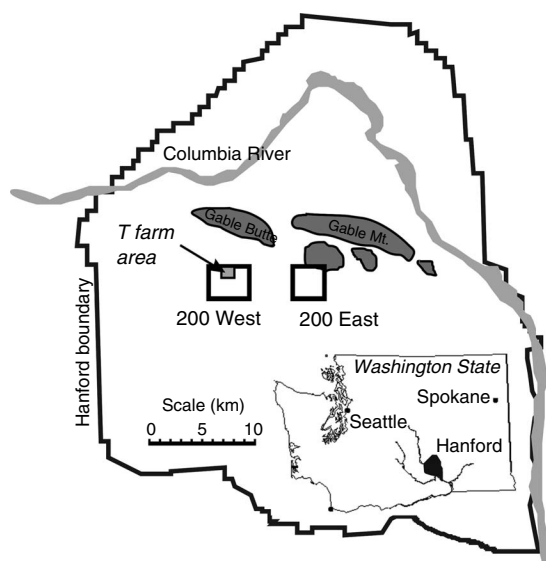


Figure 1. Location of the Hanford site, Washington, U.S.A.

farm by the T-7 crib, which was used from 1948 to 1955. Figure 2 shows the disposal volumes for all of the waste facilities. The waste was delivered to the vadose zone at T-7 by a distributed piping system that created a large leach field. The waste was primarily composed of nitrate with a concentration of 0.98 mol/liter. The T-32 crib received about one-third of the waste volume of crib T-7, but the nitrate concentration was higher at 1.38 mol/liter. The concentration of the nitrate disposed in the northeastern trenches (T-14 through T-17) was approximately 1.72 mol/liter.

**Geologic description**

The Hanford site is located within the Pasco basin of the Columbia Plateau in southeastern Washington State. The plateau is a broad plain underlain by a thick sequence of basalt flows (the Columbia River Basalt Group) more than 3000 m thick (Paillet and Kim, 1987). The basalt flows have been folded and faulted, creating broad structural and topographic basins.

Sediments underlying the Hanford site are glaciofluvial as a result of great floods that swept through the Columbia basin during the past 15,000 years (Gee et al., 2007). Figure 3 shows a cross section from a series of borehole logs and describes stratigraphic sequences taken from west to east through the T tank farm (cross section identified in Figure 2). The major formations, from top to bottom, include the Hanford Formation, the Cold Creek unit, and the Ringold Formation. Within the tank farm’s boundaries, a reworked gravelly sand backfill from the excavation was placed around the buried tanks. Minor stratigraphic units have also been identified locally within the sandy Hanford Formation; they depend on the amount of gravel present with no clear identifying markers (Last et al., 2007). Interbedded layers of silt are also encountered and are typically laterally discontinuous. The Cold Creek unit, below the Hanford Formation, is comprised mainly of a silt over a calcium carbonate-rich caliche. The Ringold Formation is a sedimentary sequence of fluvialacus-

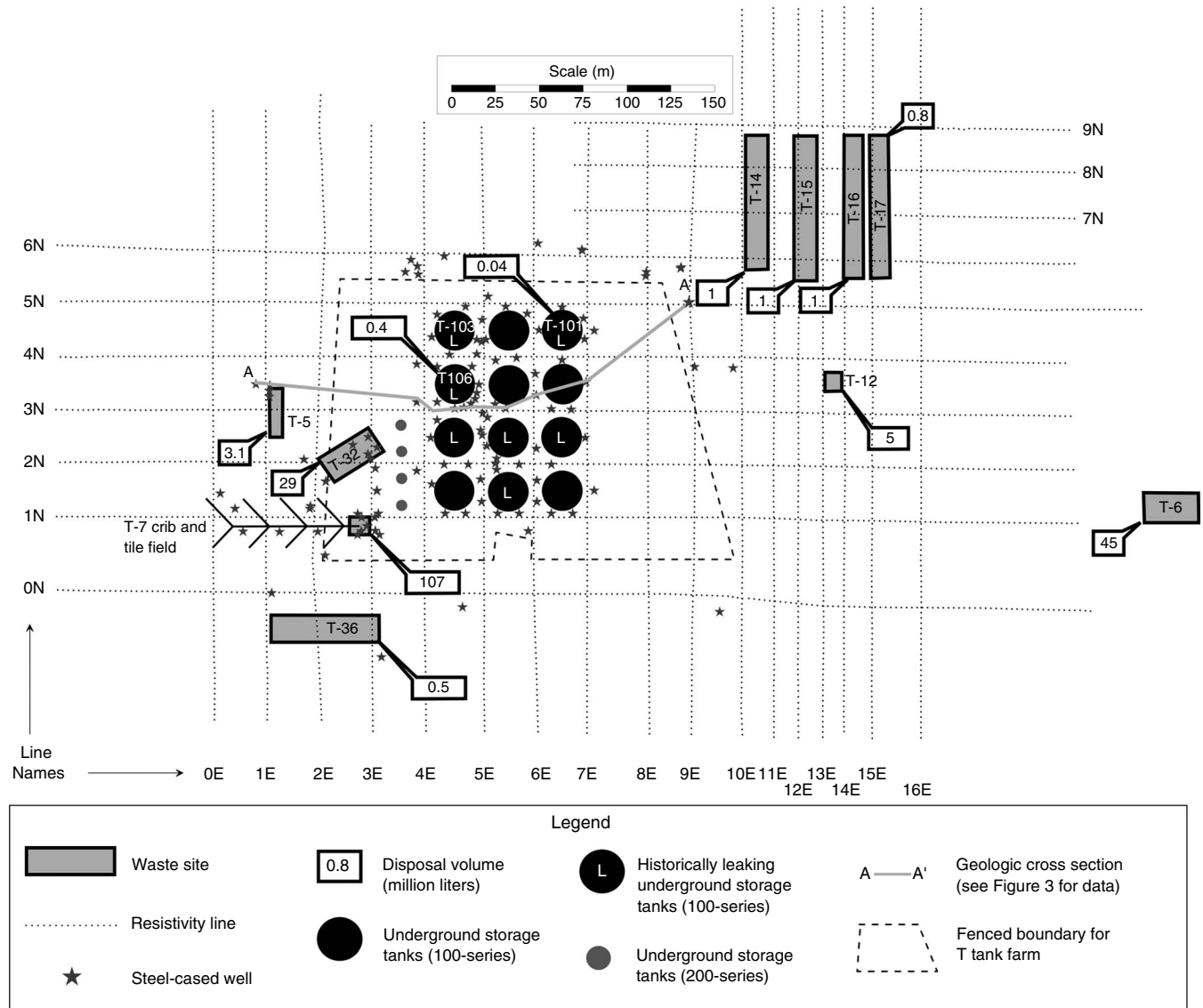


Figure 2. The T tank-farm layout. The tanks are identified as competent or potential leakers. Other liquid-waste-disposal facilities are identified with the amount of waste received. A cross section through the farm from west to east is detailed in Figure 3. The electrical-resistivity survey includes surface lines and steel wells used in a long-electrode, well-to-well inversion.

trine clay, silt, sand, and granule-to-cobble gravel deposited by the ancestral Columbia River and its tributaries (Oostrum et al., 2007).

**Hydrogeologic description**

Moisture in the vadose zone is typically concentrated along high-contrast bed interfaces as well as on finer-grained, relatively impermeable layers within the Hanford Formation and Cold Creek unit

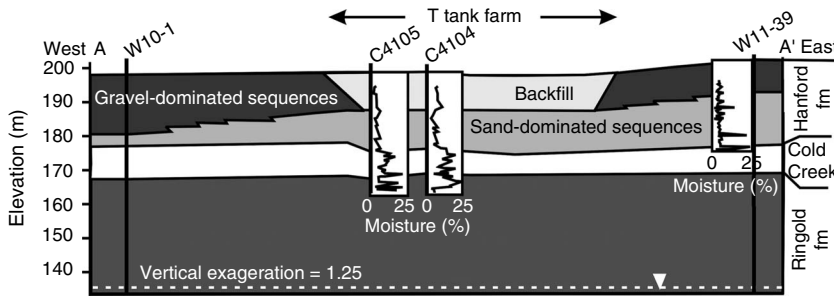


Figure 3. Cross section through the T tank farm, showing generalized geology. Moisture logs are also shown for boreholes C4104, C4105, and W11-39. Figure adapted from Myers (2005).

(DePaolo et al., 2004). Figure 3 shows moisture-profile data from several boreholes across the site. The data were derived from core samples that were oven dried to obtain gravimetric moisture content. Boreholes C4104 and C4105 were drilled through the plume resulting from the large T-106 tank leak. Borehole W11-39 was drilled to the east of the tank farm in an area thought to be undisturbed and free from contamination. The moisture data show a relatively low water content in the Hanford Formation except along thin strands of the finer-grained layers. The Cold Creek unit is marked in these profiles by an increase in moisture.

**THEORY**

The modern application of ERC uses numerical modeling and inversion theory to estimate the electrical-resistivity distribution of the subsurface from the acquired data set. Inverse modeling is necessary because measuring the resistivity is not a direct process. The acquired data set only contains positions of the electrodes and the measured potential normalized to the injected current.

However, the potential values are a result of the spatial-resistivity distribution, allowing them to

be used indirectly to back-calculate with an inversion algorithm — an estimate of the true resistivity that gives rise to those potential measurements.

A common resistivity inversion method used in commercial codes is the regularized least-squares optimization method (Sasaki, 1989; Loke et al., 2003). The objective function aims to minimize the difference between measured and modeled potentials or apparent resistivities (subject to certain constraints); the optimization is conducted iteratively as a result of the nonlinear nature of the model that describes the potential distribution. The relationship between the subsurface conductivity  $\sigma$  and the measured potential  $\phi$  is given by (Dey and Morrison, 1979)

$$-\nabla \cdot [\sigma(x,y,z) \nabla \phi(x,y,z)] = \left(\frac{I}{U}\right) \delta(x-x_s) \delta(y-y_s) \delta(z-z_s), \quad (1)$$

where  $I$  is the current applied over an elemental volume  $U$  specified at a point  $(x_s, y_s, z_s)$  by the Dirac delta function. Common methods of solving equation 1 include the finite-difference method (Dey and Morrison, 1979), the finite-element method (Sasaki, 1989; Greenhalgh et al., 2009), the analytical-element method (Furman et al., 2002), and the finite-volume approach (Pidlisecky et al., 2007). We used the finite-difference method in our research.

Regardless of the numerical method, a mesh is created whereby the subsurface is discretized into blocks and nodes. Equation 1 is solved for  $\phi$  at every node with the appropriate boundary conditions. Additional requirements of the numerical model include explicitly assigning every block a resistivity value and every node a current source (if any). Figure 4a shows a typical mesh for a 3D volume that has been discretized into rectangular blocks over several layers. Figure 4b shows a more detailed overhead view of the relationship between the mesh lines (in the  $x$ - and  $y$ -directions), model blocks, and nodes. The potentials are calculated at the nodes located at the intersections of the mesh lines, but the resistivity is assigned for the block

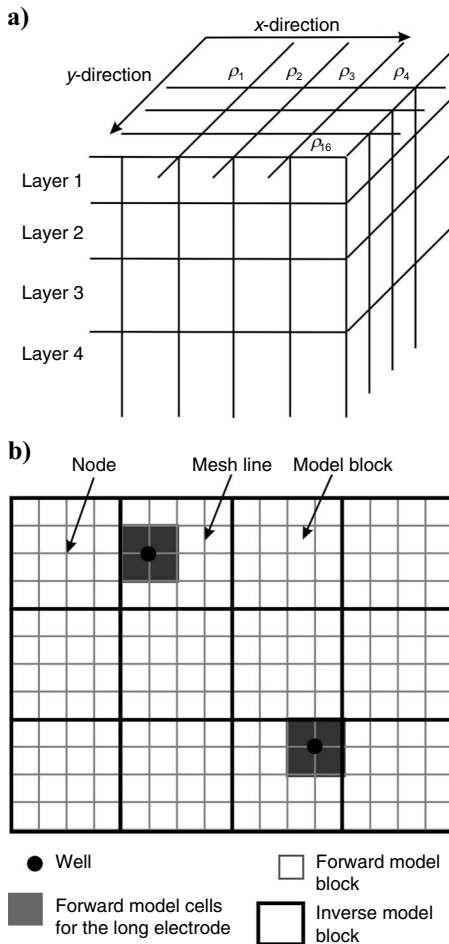


Figure 4. (a) Discretized earth for inversion and (b) overhead view of meshing, showing the relationship between nodes, mesh lines, and blocks. For the inversion code, the inverse mesh is separate from the forward mesh when using the long-electrode module.

bound by the mesh lines. Numerical methods work such that finer (or smaller) mesh sizes with more nodes give rise to more accurate solutions; the trade-off is solution efficiency and computer memory requirements.

Accommodating long electrodes in commercial resistivity modeling codes can be accomplished easily by taking advantage of the existing code structure. Although, formally, the long electrodes act as linear sources and receivers, they can be modeled with a point source on the surface and by assigning to the long electrode's position a series of very conductive cells — say, 0.01 ohm-m to simulate a metallic well. The current source is located at a node, and the adjacent four cells are assigned the low-resistivity values (Figure 4b). The high contrast between the well's resistivity and that of the surrounding medium can cause adverse effects in the numerical model such as accuracy and stability. To reduce this problem, the forward-model mesh is discretized more finely relative to the inverse-model mesh so that a more gradual transition of electrical resistivity occurs between the well and the host medium.

An example of the capability of the resistivity code is demonstrated by placing a single long electrode in a 100-ohm-m background. The numerical results of transfer resistance using the finite-difference method are compared to an analytic solution of an infinite conductor of infinitesimal diameter (from Johnston et al., 1987; Warrick and Rojano, 1999):

$$R = \frac{V}{I} = \frac{\rho}{4\pi b} \ln \left[ \frac{[r^2 + b^2]^{0.5} + b}{[r^2 + b^2]^{0.5} - b} \right], \quad (2)$$

where  $\rho$  is the resistivity of the background,  $b$  is the length of the long electrode (or well) extending from the surface of the earth, and  $r$  is the distance between the center of the well and the potential measurement location. Equation 2 can revert to the solution of a purely homogeneous half-space for  $b \rightarrow 0$ . For the numerical modeling, the length of the long electrode was simulated as 44 m. The transfer-resistance results in Figure 5 show that the resistivities of 0.01–0.001 ohm-m assigned to the long electrode produce the most accurate results. Specifically for this example, the resistivity of 0.006 ohm-m is the most accurate, with a difference of less than 4% from the analytical values for the entire distance of 1–50 m away from the well. The differences are likely partially from the assumptions of the infinite conductor and infinitesimal diameter for the analytical solution compared to the finite conductor and diameter for the numerical models.

Interestingly, the numerical results with the lowest resistivity of 0.0001 ohm-m are very inaccurate. We suspect that the contrast between the 0.0001- and the 100-ohm-m backgrounds (a resistivity contrast of 1:1,000,000) is so large that the numerical method breaks down, either from numerical round-off errors or the poor assumption of linear variation of the potential within each finite-difference cell.

The inversion of long-electrode data is similar to that presented in Loke and Dahlin (2002) and Loke et al. (2003), with the  $\ell_2$ -norm, smoothness-constrained least-squares method that aims to minimize the square of the misfit between the measured and modeled data (deGroot-Hedlin and Constable, 1990; Ellis and Oldenburg, 1994):

$$(J_i^T J_i + \lambda_i W^T W) \Delta r_i = J_i^T g_i - \lambda_i W^T W r_{i-1}. \quad (3)$$

Or the  $\ell_1$ -norm may minimize the sum of the absolute value of the misfit:

$$(J_i^T R_d J_i + \lambda_i W^T R_m W) \Delta r_i = J_i^T R_d g_i - \lambda_i W^T R_m W r_{i-1}, \quad (4)$$

where  $g$  is the data-misfit vector containing the difference between the measured and modeled data,  $J$  is the Jacobian matrix of partial derivatives,  $W$  is the roughness filter,  $R_d$  and  $R_m$  are weighting matrices to equate model misfit and model roughness,  $\Delta r_i$  is the change in model parameters for the  $i$ th iteration,  $r_i$  is the model parameters for the previous iteration  $i$ , and  $\lambda_i$  is the damping factor.

The logarithms of the model resistivity and measured apparent-resistivity values are used as the model parameters and data, respectively, in equations 3 and 4. The long-electrode module implemented in the Res3DInv x64 v3.01.24 3D resistivity inversion program (Geotomo Software, 2009) allows the wells to be located at an arbitrary grid point, separate from the discretization used for the inversion-model blocks (Figure 4b). The arbitrary grid modification simplifies the problem by eliminating the need to calculate the resistivity on a many small blocks. The following section demonstrates the inversion with long-electrode data, using the  $\ell_1$ -norm of equation 4.

## EXAMPLE MODELS

As an example of the WTW inversion method and the advantage of using wells as electrodes in infrastructure-rich areas, consider the following scenario. A simple target is placed in a 100-ohm-m background. The target is 1 ohm-m and lies 10–15 m below ground surface. The larger domain is 60 × 60 m and the target is 15 × 15 m, placed slightly off center. The pole-pole array is used for all simulations.

The results of first running the forward simulation to obtain the potential measurements and then inverting the potentials to calculate the resistivity distribution is illustrated in Figure 6. Figure 6a shows the inversion results for surface electrodes only. The surface electrodes are evenly spaced 5 m apart over the entire domain for a total of 36 electrodes and 630 measured potential values. In the figure, the higher-resistivity values are peeled away to reveal the lowest values, which range from 50 to 80 ohm-m. These values were chosen so the footprint of the inverted target matches the footprint of the original target. For reference, a transparent horizontal color-contoured layer is placed at a depth of 12 m, through the center of the original target.

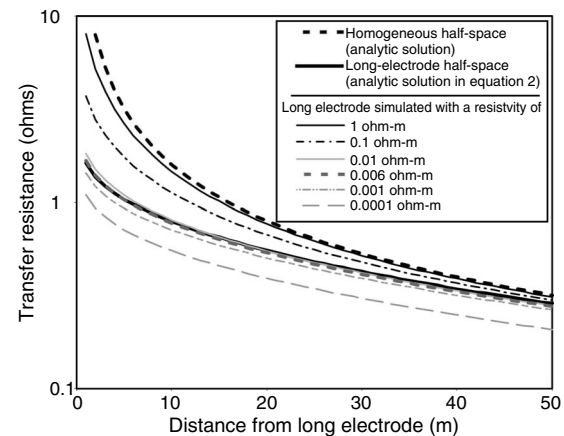


Figure 5. Numerical model results of a finite conductor of finite length and finite diameter compared to the analytic solution of an infinite conductor of infinitesimal diameter.

The inverted target matches the footprint of the original target quite well with some vertical smearing, which is common with this type of reconstruction.

Figure 6b shows the inversion results from a similar circumstance but using 20 long electrodes and no surface electrodes. The parameters of the long electrodes are the same as in Figure 5. The density of long electrodes (200 m<sup>2</sup>/electrode) for the model are meant to replicate that of inside the T tank farm (188 m<sup>2</sup>/well); the electrode arrangement places two electrodes through the target. The inversion results show a high propensity for the long-electrode technique to

replicate the target but with an elevated resistivity distribution compared to Figure 6a. Additionally, the vertical distribution of the target is funnel shaped, with most of the low-resistivity values at the surface. We surmise that the finite conductivity value used for the long electrode concentrates much of the current density nearer the surface. This fact will likely reduce vertical resolution when using the long-electrode technique in the field.

Figure 6c and d repeats the previous two models with the exception of a 0.25-m-thick high-conductivity layer (0.01 ohm-m) at a depth of 1 m. The conductive layer is meant to replicate specifically

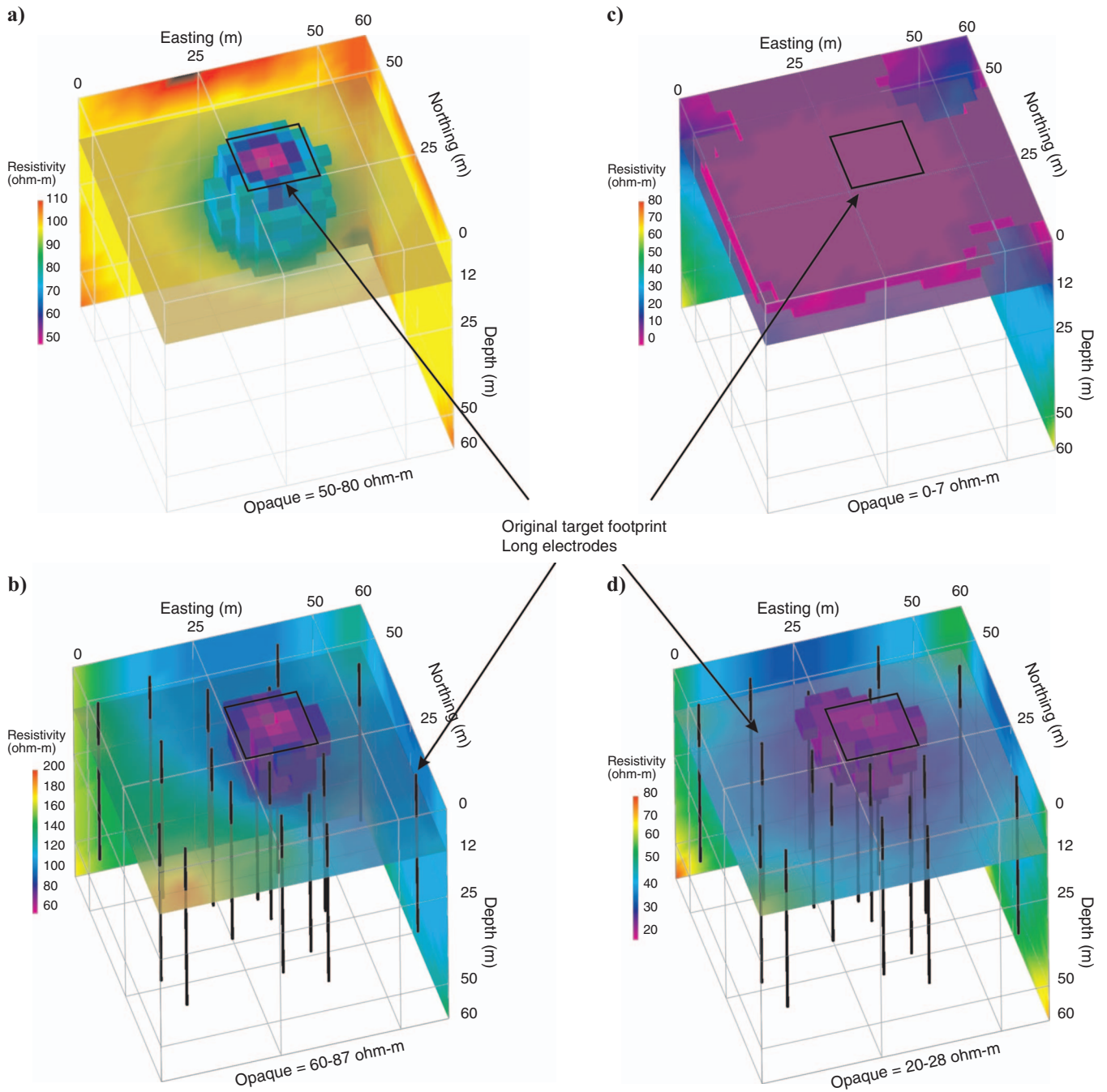


Figure 6. Example models showing the resistivity inversion results for surface and long electrodes: (a) surface electrodes with simple target, (b) long electrodes with simple target, (c) surface electrodes with simple target and conductive surface layer, (d) long electrodes with simple target and conductive surface layer. The target footprint is drawn to show the fidelity of the types of electrodes to replicate the position of the target.

the near-surface piping network, and the tanks are not accommodated in these example models. It is debatable whether the tanks, encased in concrete and asphalt, are actually electrically conductive or resistive features. Furthermore, the simulated infrastructure is slightly higher in resistivity than the well to replicate the fact that the piping would never actually touch a well. The inversion with surface electrodes shows a thin, low-resistivity layer that obliterates the target below it, making the original target indistinguishable. Although only the lowest resistivity values are shown in Figure 6c, a cycling through the complete set of data fails to reveal any information about the original target's whereabouts. The use of long electrodes in Figure 6d overcomes the conductive surface layer and makes a good attempt to reproduce the lateral position of the target. The long-electrode results with a surface layer lower the overall resistivity values of the target and background compared to Figure 6a and b.

Therefore, limitations can be expected with the long-electrode technique when applying petrophysical models for estimations of moisture content or salt concentration because the resistivity of the inverted target will depend on the amount of infrastructure and number of wells. The long-electrode method should be applied more as a target-recognition technique.

## ACQUISITION METHODOLOGY AT THE TANK FARM

We now demonstrate two methods of ERC deployment tested at the T tank farm, using field data acquired at Hanford. The first method involves surface electrodes placed along linear transects to obtain profiles of the subsurface. The lines are placed in parallel and orthogonal directions. The second method uses steel wells as long electrodes distributed unevenly around the tank farm, with wells acting as transmitters and receivers. A SuperSting<sup>®</sup> R8 (Advanced Geosciences, Inc.) resistivity meter collects the data; the system is capable of measuring the voltage of eight pairs of electrodes simultaneously.

The pole-pole array is used for both methods of deployment, with the receiver remote located 1300 m northwest of the northern portion of the tank farm fence and the transmitter remote located 1900 m to the northeast. A pole-pole array is chosen for the surface lines, based on its ability to resolve deeper targets with shorter lines compared to other array types. Additionally, the pole-pole electrode arrangement is chosen for the long electrodes based on the manageable number of possible measurements compared to pole-bipole and bipole-bipole arrangements.

### Surface ERC

Data acquisition for the surface ERC commenced on 10 June 2005 and was completed on 27 July 2005. A total of 27 transects were used to cover the tank farm and the surrounding cribs and trenches, with 10 lines running east-west (0N–9N) and 17 lines running north-south (0E–16E). The parallel lines were spaced roughly 15 or 30 m apart, depending on spatial distribution of waste sites and tanks. In general, lines running through the farm were placed so they did not go directly over a tank. Outside the farm, lines were placed to go over and between liquid-waste-disposal sites. Figure 2 shows the layout of the surface-resistivity survey, which summed to 12 line-km over a 23-ha area. The individual lines were composed of an initial 155-electrode setup with an intraline electrode spacing of 3 m. This setup, stretching 465 m, had a maximum A-spacing (distance between

transmitting and receiving electrode) of 360 m. The roll-along technique was then used to extend the line to more than 680 m in some cases. The roll-along advanced the resistivity line 72 electrodes per move.

The individual line lengths ranged from 283 m (for 7N–9N) to 686 m (for 6N). Raw data acquisition averaged nine data points per meter of line acquisition. After removing noise spikes, the remaining data count for all lines was approximately 103,000.

### Well-to-well ERC

Data acquisition for the WTW ERC was performed between 20 January 2006 and 25 January 2006. Figure 2 shows the distribution of wells used for the WTW survey. The steel wells included 93 that were completed in the vadose zone (<70 m long) and 17 completed to groundwater (up to 93 m long). Most wells are within the tank-farm fence and are arranged around each tank. These wells are used for periodic borehole geophysical logging, including neutron probe and spectral gamma ray, to detect potential leaks from the aging tanks (Henwood and McCain, 2006).

The wells typically range from 10 to 20 cm in diameter, and most (if not all) were drilled with a cable-tool rig. Of the 11,990 possible combinations of transfer-resistance measurements (including reciprocals) on the 110 wells with the pole-pole array, 10,635 were retained after the first rejection criteria by the resistivity meter; rejection is based on high repeat errors. The remaining data are presented in Figure 7 as transfer resistance (in ohms) versus distance between well pairs. The slope of the trend line through the data is  $-0.78$ , which is close to that of point electrodes on the surface over a homogeneous earth (which is  $-1$ ).

## RESULTS

### Surface ERC

The data obtained with the surface electrodes were processed in two and three dimensions. The 2D profiles were inverted using the methodology according to Loke and Barker (1996) and Loke et al. (2003). Figure 8 shows two example profiles that run over the liquid-waste disposal sites on the periphery of the tank farm or were collected through the tank farm (lines 3E and 1N, respectively). For line 3E of Figure 8a, the inversion starts with a homogeneous resistivity distribution equivalent to the average apparent resistivity and completes in three iterations to a final rms error of 4.61%. The low number of iterations and low rms error indicate low noise in the data set.

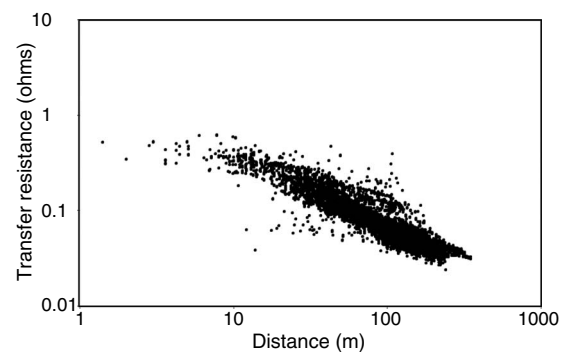


Figure 7. Well-to-well data collected with the pole-pole array at the T tank farm, with transfer resistance versus distance between well pairs.

The line shows several low-resistivity targets that correspond to the location of waste sites. The feature beneath the T-7 leach field, in particular, shows a low-resistivity plume developed from the historical disposal activities. The approximate location of the water table is also shown at a depth of 70 m and indicates contamination has possibly reached the groundwater. Nearby groundwater monitoring wells have measured nitrate and other contaminants (Myers, 2005).

The inversion results of line 1N in Figure 8b show a wide range of resistivity values (six orders of magnitude). The most conductive features are found in areas adjacent to and east of the tanks, where a large piping network, distribution boxes, and manifold system were buried to effectively distribute the waste from the chemical processing plant to the tanks. The inversion statistics are telling as well, with a final rms of 21.5% after six iterations. The line is highly noisy, and the low-resistivity features may actually be the result of subsurface infrastructure, not tank leaks. The results are typical of those that run through the tank farm and are considered uninterpretable, based on the potential interference with metal.

Given that the west side of the tank farm is relatively free from metal, a 3D inversion was completed for the entire west side using data up to (and including) line 3E. Figure 9 shows the inversion results as a horizontal slice of color contours 30 m below the ground surface. The inversion was completed in five iterations to a final rms of 8.51%. The data show a low-resistivity target concentrated directly below the T-32 and T-7 cribs. The low-resistivity values extend westward to include the area beneath most of the distribution piping, from T-7 and northward to the west of T-5. From a hydrogeologic perspective, the location and lateral extent fits with expectations, given the amount of waste disposed in the region.

**Well-to-well ERC**

The apparent resistivity data from wells in the tank farm were used as input for the inversion model; the calculated resistivity dis-

tribution is displayed in Figure 10. The WTW results use the same color contouring as Figures 8 and 9 for direct comparison with surface ERC, and the WTW data are shown as a horizontal depth slice at 1.4 m. The apparent resistivity was calculated assuming the geometric factor from surface electrodes with poles at infinity. Although this is known to be an incorrect formulation, its choice is inconsequential to the model results because any geometric factor would be a constant throughout the inverse procedure.

Other input to the inversion code included explicitly defining the position, length, and diameter of almost every well. Some wells in the tank farm were eliminated from the inversion because of their close proximity to other wells or were out of bounds for a reasonable model domain, leaving 87 of the original 110 wells and 6522 measured data values. The position and length were easily determined from historical records, and the diameter for all wells was given a value of 0.1 m. An arbitrary mesh for inversion was established on a 4-m grid to create 70,308 inverse model blocks. We used an arrangement whereby each inverse model block was covered by four mesh lines in the *x*- and *y*-directions, resulting in a forward mesh composed of 2,466,750 blocks. In the vertical direction, a finer mesh spacing was used near the surface, with an increasingly coarser mesh for each deeper layer.

The WTW ERC data show several low-resistivity targets around known disposal areas. The most significant target is found in the southwest corner of the grid around cribs T-5, T-7, and T-32. Given the large volume of disposal, this target matches hydrogeologic expectations. The exact shape and position of the large target, however, are likely influenced by the distribution and density of the electrodes. When comparing WTW to the 3D surface ERC, we see the low-resistivity plume extending beneath the leach field in both models.

Another significant target is found at the southeast corner of tank T-106, which matches the conceptual model discussed in Myers

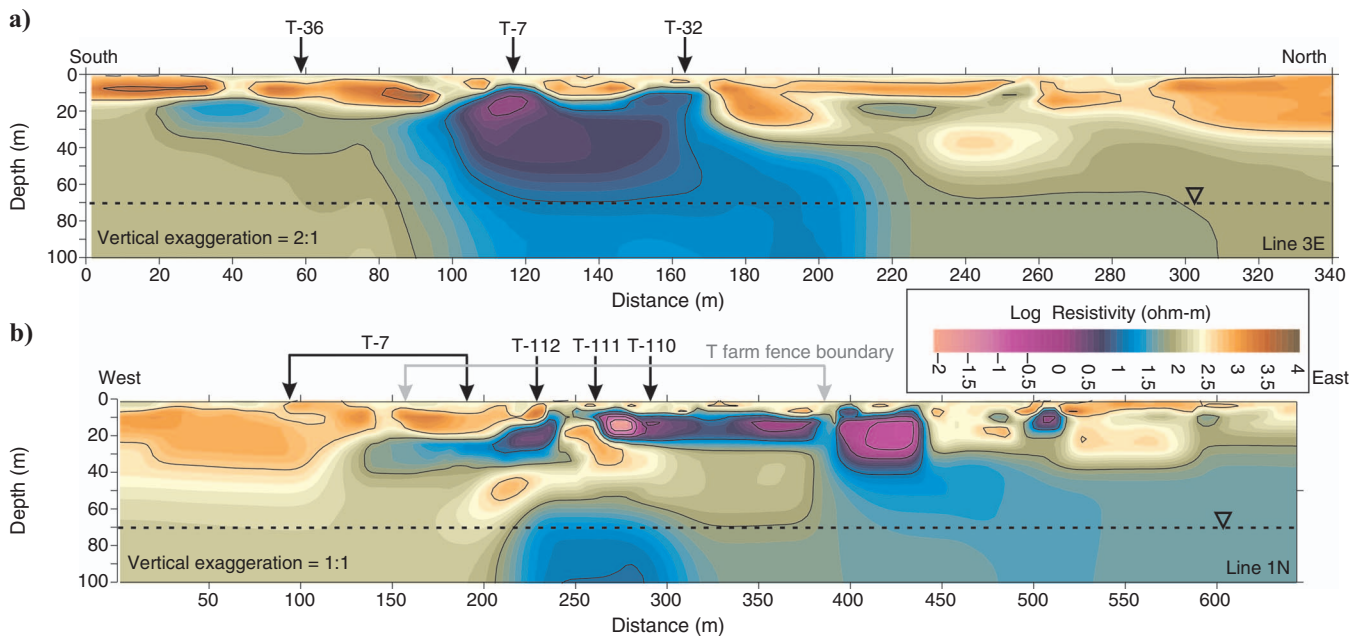


Figure 8. Example 2D lines at the tank farm. (a) Line 3E in the western region of the farm over several waste disposal facilities. (b) Line 1N placed directly through the infrastructure-rich tank farm.

(2005). In general, this target is elongated from the northwest corner of T-106 (and directly south of T-103) to the northwest corner of T-111. Other targets in the tank farm include a low-resistivity feature south of T-101 that also matches the conceptual hydrogeologic models. A target that may be unsubstantiated is north of the tank-farm fence, associated with a single well. The region north of the tanks has few wells, and the final resistivity distribution in this area must be viewed with this fact in mind. Similarly, the outer periphery of the larger model domain, especially the northeast corner, has no wells, making the calculated resistivity values highly suspect.

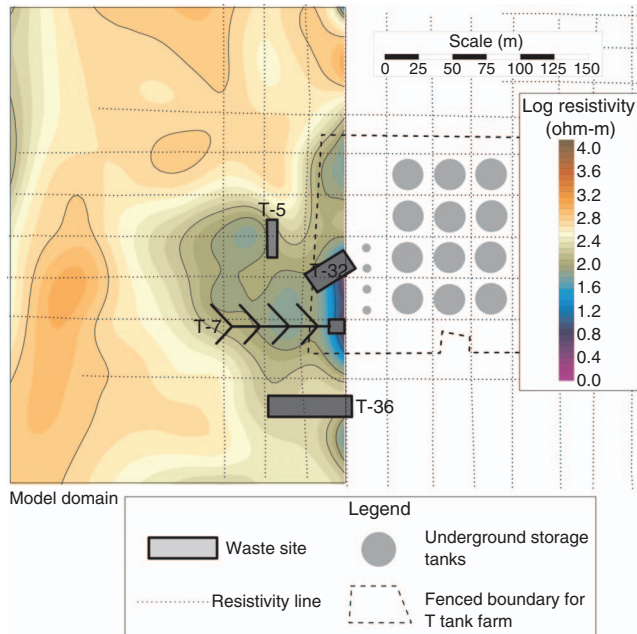


Figure 9. The 3D electrical-resistivity inversion results for the western region of the tank farm.

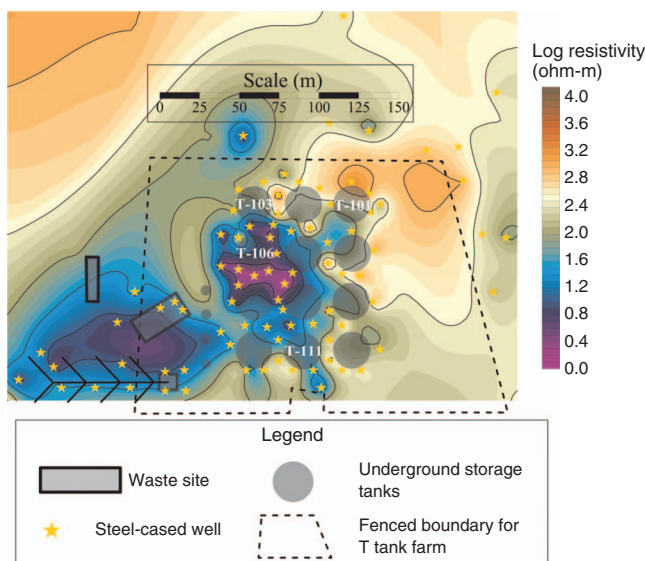


Figure 10. Well-to-well electrical-resistivity inversion results for the tank farm.

## CONCLUSION

An ERC study was completed using point electrodes on the surface of the earth and steel wells extending below the surface as long electrodes. The study included (1) comparisons of the numerical solution to an analytical solution with a single transmitting long electrode and receiving point electrodes on the surface, (2) hypothetical inverse-modeling examples with a simple target, and (3) field data collected at the T tank farm in the 200 West area of the Hanford site. Numerically, the finite-difference method was used in the resistivity model to simulate the transfer resistance acquired from long electrodes. Long electrodes were explicitly accommodated in the model by assigning low-resistivity values to the model blocks representing the electrode's location.

The analytical solution used to validate the potential field from a transmitting long electrode in the numerical model was derived based on an infinite conductor of infinitesimal diameter. Although these assumptions are not accommodated in the numerical model, the comparison showed that the numerical model could be fairly accurate when using a well resistivity value of 0.006 ohm-m in a 100-ohm-m background. The difference between the two solutions was less than 4% up to 50 m away from the well, with an average of 2.75% difference over the model domain.

The hypothetical modeling examples were designed to test the strength of a long-electrode survey where a near-surface metallic infrastructure potentially could mask any subsurface contaminant plume using a surface array. The modeling first compared the results of a survey using only surface point electrodes to a survey using only long electrodes for a simple target buried 10–15 m below the ground surface in an otherwise homogeneous background. The surface-electrode array recreated, with higher fidelity, the original target location than the long-electrode array, suggesting that the surface-electrode array is preferable in this situation. The results of the long-electrode array did, however, locate the target in the  $x$ - $y$ -plane, but the depth information was lost.

The second hypothetical model placed a thin, conductive layer above the simple target and just below the surface to replicate metallic infrastructure, such as a piping network. The same electrode set-up for point and long electrodes was used as in the first example. The results showed that the target estimated with the surface-electrode array could not be differentiated from the conductive near-surface layer; the near-surface layer appeared to obliterate information below it. The results of the long-electrode array recreated with reasonable accuracy the location of the simple target. The near-surface layer reduced the overall range of resistivity values estimated by the long-electrode array compared to the situation of no near-surface layer, but the target was in the correct location.

The resistivity field campaign at the T tank farm included surface electrodes and wells, with the objective to compare the results of the surface array to that of the WTW array in areas of no infrastructure. The western area of the tank farm received more than  $140 \times 10^6$  liters of liquid electrolytic waste (mostly sodium nitrate) in several waste disposal facilities, and surface and long-electrode surveys identified a large, low-resistivity target beneath these facilities. The shape of the target is different in the two surveys, likely because of the well coverage and density in the area. Based on the similarities of the two surveys outside the tank farm, we reasoned that the location of targets inside the tank farm could be estimated with the WTW technique. Conceptual models and known information about historical leaks from tanks placed a plume to the southwest of tank T-106.

The WTW results showed a large resistivity low in the area that extended to the southernmost row of tanks. Other smaller targets were also identified that appeared to correlate with suspected tank releases. Based on these results, the WTW resistivity method provides a possible new strategy of environmental characterization at highly industrialized sites, provided a sufficient number and density of wells exist.

### ACKNOWLEDGMENTS

Special thanks go to Dave Myers of Washington River Protection Solutions for reviewing the paper. We also thank Michael McNeill, Chris Baldyga, Kraig Williams, and Matt Switanek for data acquisition.

### REFERENCES

- Bauer, P., R. Supper, S. Zimmermann, and W. Kinzelbach, 2006, Geoelectrical imaging of groundwater salinization in the Okavango delta, Botswana: *Journal of Applied Geophysics*, **60**, 126–141.
- Bevc, D., and H. F. Morrison, 1991, Borehole-to-surface electrical resistivity monitoring of a salt water injection experiment: *Geophysics*, **56**, 769–777.
- Cassiani, G., V. Bruno, A. Villa, N. Fusi, and A. M. Binley, 2006, A saline trace test monitored via time-lapse surface electrical resistivity tomography: *Journal of Applied Geophysics*, **59**, 244–259.
- Choudhury, K., D. K. Saha, and P. Chakraborty, 2001, Geophysical study for saline water intrusion in a coastal alluvial terrain: *Journal of Applied Geophysics*, **46**, 189–200.
- Daily, W., A. Ramirez, and A. Binley, 2004a, Remote monitoring of leaks in storage tanks using electrical resistance tomography: Applications at the Hanford site: *Journal of Environmental and Engineering Geophysics*, **9**, 11–24.
- Daily, W., A. Ramirez, R. Newmark, and K. Masica, 2004b, Low-cost reservoir tomographs of electrical resistivity: *Leading Edge*, **23**, 472–480.
- deGroot-Hedlin, C., and S. C. Constable, 1990, Occam's inversion to generate smooth, two-dimensional models from magnetotelluric data: *Geophysics*, **55**, 1613–1624.
- DePaolo, D. J., M. E. Conrada, K. Maherb, and G. W. Gee, 2004, Evaporation effects on oxygen and hydrogen isotopes in deep vadose zone pore fluids at Hanford, Washington: *Vadose Zone Journal*, **3**, 220–232.
- Dey, A., and H. F. Morrison, 1979, Resistivity modeling for arbitrarily shaped three-dimensional shaped structures: *Geophysics*, **44**, 753–780.
- Ellis, R. G., and D. W. Oldenburg, 1994, Applied geophysical inversion: *Geophysical Journal International*, **116**, 5–11.
- Furman, A., A. W. Warrick, and T. P. A. Ferré, 2002, Electrical potential distributions in response to applied current in a heterogeneous subsurface — Solution for circular inclusions: *Vadose Zone Journal*, **1**, 273–280.
- Gee, G. W., M. Oostrom, F. D. Freshley, M. L. Rockhold, and J. M. Zachara, 2007, Hanford site vadose zone studies: An overview: *Vadose Zone Journal*, **6**, 899–905.
- Geotomo Software, 2009, Instruction manual for Res3DInv x64, version 3.01: Rapid 3D resistivity and IP inversion using the least-squares method, <http://www.geoelectrical.com/downloads.php>, accessed 24 June 2010.
- Gephart, R. E., 2003, Hanford: A conversation about nuclear waste and cleanup: Battelle Press.
- Greenhalgh, S. A., B. Zhou, M. Greenhalgh, L. Marescot, and T. Wiese, 2009, Explicit expressions for the Fréchet derivatives in 3D anisotropic resistivity inversion: *Geophysics*, **3**, no. 3, F31–F43.
- Hanlon, B. M., 2005, Waste tank summary report for the month ending February, 28, 2006: Fluor Hanford Contractor's report HNF-EP-0182 rev 203, [http://www5.hanford.gov/pdw/fsd/AR/FSD0001/FSD0013/D7686970/D7686970\\_25674\\_41.pdf](http://www5.hanford.gov/pdw/fsd/AR/FSD0001/FSD0013/D7686970/D7686970_25674_41.pdf), accessed 24 June 2005.
- Henwood, P. D., and R. G. McCain, 2006, Discrimination of radionuclides in high-resolution spectral gamma logging: Proceedings of the 2006 Waste Management Symposium.
- Johnston, R. H., F. N. Trofimenkoff, and J. W. Hasslett, 1987, Resistivity response of a homogeneous earth with a finite-length contained vertical conductor: *IEEE Transactions on Geoscience and Remote Sensing*, **GE-25**, 414–421.
- Koukadaki, M. A., G. P. Karatzas, M. P. Papadopoulou, and A. Vafidis, 2007, Identification of the saline zone in a coastal aquifer using electrical tomography data and simulation: *Water Resources Management*, **21**, 1881–1898.
- LaBrecque, D. J., G. Heath, R. Sharpe, and R. Versteeg, 2004, Autonomous monitoring of fluid movement using 3-D electrical resistivity tomography: *Journal of Environmental and Engineering Geophysics*, **9**, 167–176.
- Last, G. V., C. J. Murray, D. A. Bush, E. C. Sullivan, M. L. Rockhold, R. D. Mackley, and B. N. Bjornstad, 2007, Standardization of borehole data to support vadose zone flow and transport modeling: *Vadose Zone Journal*, **6**, 906–912.
- Loke, M. H., I. Acworth, and T. Dahlin, 2003, A comparison of smooth and blocky inversion methods in 2D electrical imaging surveys: *Exploration Geophysics*, **34**, 182–187.
- Loke, M. H., and R. D. Barker, 1996, Rapid least-squares inversion of apparent resistivity pseudo-sections using quasi-Newton method: *Geophysical Prospecting*, **44**, 131–152.
- Loke, M. H., and T. Dahlin, 2002, A comparison of Gauss-Newton and quasi-Newton methods in resistivity imaging inversion: *Journal of Applied Geophysics*, **49**, 149–162.
- Myers, D. A., 2005, Field investigation report for waste management areas T and TX-TY, rev. 0-A: Hill Hanford Group Contractor's Report RPP-23752, [http://www5.hanford.gov/pdw/fsd/AR/FSD0001/FSD0054/1001051156/\[1001051145\].pdf](http://www5.hanford.gov/pdw/fsd/AR/FSD0001/FSD0054/1001051156/[1001051145].pdf), accessed 24 June 2010.
- Nowroozi, A. A., S. B. Horrocks, and P. Henderson, 1999, Saltwater intrusion into the freshwater aquifer in the eastern shore of Virginia: A reconnaissance electrical resistivity survey: *Journal of Applied Geophysics*, **42**, 1–22.
- Oostrom, M., M. L. Rockhold, P. D. Thorne, M. J. Truex, G. V. Last, and V. J. Rohay, 2007, Carbon tetrachloride flow and transport in the subsurface of the 216-Z-9 trench at the Hanford site: *Vadose Zone Journal*, **6**, 971–984.
- Paillet, F. L., and K. Kim, 1987, Character and distribution of borehole break-outs and their relationship to in situ stresses in deep Columbia River basalts: *Journal of Geophysical Research*, **92**, no. B7, 6223–6234.
- Pidlisecky, A., E. Haber, and R. Knight, 2007, RESINVM3D: A 3D resistivity inversion package: *Geophysics*, **72**, no. 2, H1–H10.
- Pidlisecky, A., R. Knight, and E. Haber, 2006, Cone-based electrical resistivity tomography: *Geophysics*, **71**, no. 2, G157–G167.
- Ramirez, A., W. Daily, A. Binley, D. LaBrecque, and D. Roelant, 1996, Detection of leaks in underground storage tanks using electrical resistance methods: *Journal of Environmental and Engineering Geophysics*, **1**, 189–204.
- Ramirez, A. L., R. L. Newmark, and W. D. Daily, 2003, Monitoring carbon dioxide floods using electrical resistance tomography (ERT): Sensitivity studies: *Journal of Environmental and Engineering Geophysics*, **8**, 187–208.
- Rucker, D. F., 2010, The application of magnetic gradiometry and electromagnetic induction at a former radioactive waste disposal site: *Waste Management and Research*, **28**, 364–372.
- Rucker, D. F., and J. B. Fink, 2007, Inorganic plume delineation using surface high-resolution electrical resistivity at the BC cribs and trenches site, Hanford: *Vadose Zone Journal*, **6**, 946–958.
- Rucker, D. F., J. B. Fink, M. T. Levitt, D. R. Glaser, and C. A. Baldyga, 2005, High resolution resistivity (HRR) delineation of a liquid waste plume at a former radioactive waste disposal site, Hanford, Washington: Proceedings of the 2005 Waste Management Symposium.
- Rucker, D. F., M. T. Levitt, and W. J. Greenwood, 2009, Three-dimensional electrical resistivity model of a nuclear waste disposal site: *Journal of Applied Geophysics*, **69**, 150–164.
- Rucker, D. F., M. T. Levitt, C. Henderson, and K. Williams, 2006, Surface geophysical exploration of T tank farm: Hill Hanford Group Contractor's Report RPP-RPT-28955, CH2M, [http://www5.hanford.gov/pdw/fsd/AR/FSD0001/FSD0054/1001051159/\[1001051159\].pdf](http://www5.hanford.gov/pdw/fsd/AR/FSD0001/FSD0054/1001051159/[1001051159].pdf), accessed 24 June 2010.
- Sasaki, Y., 1989, Two-dimensional joint inversion of magnetotelluric and dipole-dipole resistivity data: *Geophysics*, **54**, 254–262.
- Singha, K., and S. M. Gorelick, 2005, Saline tracer visualized with three-dimensional electrical resistivity tomography: Field-scale spatial moment analysis: *Water Resources Research*, **41**, W05023.
- , 2006, Effects of spatially variable resolution on field-scale estimates of tracer concentration from electrical inversions using Archie's law: *Geophysics*, **71**, no. 3, G83–G91.
- Swarzenski, P. W., F. W. Simonds, A. J. Paulson, S. Kruse, and C. Reich, 2007, Geochemical and geophysical examination of submarine groundwater discharge and associated nutrient loading estimates into lynch cove, Hood Canal, WA: *Environmental Science and Technology*, **41**, 7022–7029.
- Vickery, A. C., and B. A. Hobbs, 2002, The effects of subsurface pipes on apparent resistivity measurements: *Geophysical Prospecting*, **50**, 1–13.
- Waite, J. L., 1991, Tank wastes discharged directly to the soil at the Hanford site: Westinghouse Hanford Contractor's Report WHC-MR-0227, [http://www5.hanford.gov/pdw/fsd/AR/FSD0001/FSD0040/D196059556/D106959556\\_5926\\_52.pdf](http://www5.hanford.gov/pdw/fsd/AR/FSD0001/FSD0040/D196059556/D106959556_5926_52.pdf), accessed 24 June 2010.
- Warrick, A. W., and A. Rojano, 1999, Effects of source cavity shape on steady, three-dimensional flow of soil gases: *Water Resources Research*, **35**, 1425–1433.
- Zachara, J. M., J. Serne, M. Freshley, F. Mann, F. Anderson, M. Wood, T. Jones, and D. Myers, 2007, Geochemical processes controlling migration of tank wastes in Hanford's vadose zone: *Vadose Zone Journal*, **6**, 985–1003.